An In-Depth Correlation of the Perturbation of the Organic–Inorganic Interface Topology, Electronic Structure, and Transport Properties within an Extended Series of 21 Metallic Pseudopolymorphs, β''-(BEDT-TTF)$_4$·(guest)$_n$·[$Re_6Q_6Cl_8$], (Q = S, Se)

André Deluzet,[a] Roger Rousseau,[b, d] Christophe Guilbaud,[a] Isabelle Granger,[c] Kamal Boubekeur,[a, e] Patrick Batail,*[a, e] Enric Canadell,*[b] Pascale Auban-Senzier,[c] and Denis Jérôme[c]

Dedicated to Professor Fred Wudl on the occasion of his 60th birthday

Abstract: An in-depth analysis of a set of 21 layered structures of metallic pseudopolymorphs of general formulation, β''-(BEDT-TTF)$_4$·(guest)$_n$·[$Re_6Q_6Cl_8$], (BEDT-TTF = bis-ethylenedithiotetrathiafulvalene; Q = S, Se; guest = H_2O, 1,4-dioxane, THF, CCl_4, C_2H_5OH, $CHCl_3$, CH_2ClI, CH_2ClBr, CH_2Cl_2, CH_2OH-CH_2OH, C_5H_5N, CH_3COCH_3, 2-hydroxy-tetrahydrofuran, CH_3CN, CS_2, C_6H_6), with diverse low-temperature behaviors, which differ solely by the nature of the cosolvent molecule selectively included during the electrocrystallization process, reveals a precise set of weak HO-H···Cl-μ-Re, $(C\text{-}H)_{BEDT\text{-}TTF}$···Cl-$\mu$-Re, C-H···$O_{guest}$, $(C\text{-}H)_{guest}$···Cl-μ-Re hydrogen bonds at the organic–inorganic interface, none of which dominates any of the others and whose balance is adjusted upon substitution of one guest molecule by another. The electronic structure of the host adjusts to the weak perturbation imposed by exchanging the guest molecules and by balancing the former interfacial interactions; this correlates to a net activation of up to 0.1 eV of the energy of the HOMO level of one of the two donors, while keeping the pattern of HOMO–HOMO intermolecular interactions in the donor layer essentially unaltered. It is suggested that this controls the stability of the metallic state at low temperature or the occurrence of a metal-to-insulator phase transition for particular guests along the series. It is concluded that by allowing for numerous tiny modifications at the organic–inorganic interface within a single, robust host structure, one sees a concerted, inherently weak structural response of the system that is proportional to the magnitude of the underlying, equally weak activation of the HOMO energy of a fraction of the π-donor molecules within the slabs; this has a sizeable influence on the macroscopic transport properties of the system.

Keywords: cluster compounds · hydrogen bonds · metallic materials · organic–inorganic interface · radical ions

Introduction

We report here on accurate crystal structures of the title pseudopolymorphs, a large series of ternary radical cation hybrid salts. They were constructed in order to learn how to decipher the organic–inorganic interface topology and its subtle adjustment to weak perturbations by different neutral guest molecules and to understand how these relate to the

[a] Dr. P. Batail, Dr. A. Deluzet, Dr. C. Guilbaud, Dr. K. Boubekeur
Laboratoire Sciences Moléculaires aux Interfaces
CNRS FRE 2068, Institut Jean Rouxel
2 rue de la Houssinière, 44322 Nantes (France)

[b] Dr. E. Canadell, Dr. R. Rousseau
Institut de Ciència de Materials de Barcelona (CSIC)
Campus de la U. A. B. 08193 Bellaterra (Spain)
Fax: (+34) 935 805 729
E-mail: canadell@icmab.es

[c] I. Granger, Dr. P. Auban-Senzier, Dr. D. Jérôme
Laboratoire de Physique des Solides, Bât. 510
Université de Paris-Sud, 91405 Orsay Cedex (France)

[d] Dr. R. Rousseau
Present address: Lehrstuhl für Theoretische Chemie
Ruhr-Universität-Bochum
44780 Bochum (Germany)

[e] Dr. P. Batail, Dr. K. Boubekeur
Present address:
Laboratoire Chimie Inorganique, Matériaux et Interfaces
FRE 2447, CNRS-Université d'Angers, Bât. K, UFR Sciences
2, Boulevard Lavoisier, 49045 Angers (France)
Fax: (+33) 2-41-73-50-11
E-mail: patrick.batail@univ-angers.fr

Supporting information for this article is available on the WWW under http://www.chemeurj.org/ or from the author. Temperature dependence of the resistivity measured by the four point method for one single crystal of **2**, **5**–**7**, **9**, **13**, **15**, **17** and **19**. The values of the room-temperature conductivities are indicated.

0947-6539/02/0817-3884 $ 20.00+.50/0 *Chem. Eur. J.* **2002**, *8*, No. 17

electronic structure, phase diagram, and electronic instabilities within prototypical molecular solids that exhibit metallic conductivity at room temperature.

There are a number of relevant current examples in which incorporated water or organic molecules have been shown to affect the macroscopic transport properties of the materials. Thus, the replacement of tetrahydrofuran molecules by dihydrofuran molecules in (BEDT-ATD)$_2$PF$_6$·THF (BEDT-ATD = bis-ethylenedithiodihydroanthrathiadiazole) induces a metal–insulator transition at 150 K; this has been correlated to the occurrence of different models of disorder on the neutral molecule sites.[1] In the series, (BEDT-TTF)$_2$M(CF$_3$)$_4$·(CH$_2$X-CHYZ), (M = Cu, Ag, Au and X/Y/Z = Cl, Br), incorporation of similar neutral molecules, albeit with different halogen substitution patterns, results in different critical temperatures for superconductivity. In addition to the effect of disorder inherent in the versatile patterns of halogen substitutions, the different neutral molecules also have different steric demands on the organic–inorganic interface that might affect the respective transfer-integral distribution within the conducting slab.[2] The two phases, β''-(BEDT-TTF)$_4$[(H$_3$O)Fe(C$_2$O$_4$)$_3$]·solvent (benzonitrile or pyridine) have contrasting properties. The benzonitrile solvate is a superconductor (T_C = 8.6 K) whereas a metal–insulator transition, associated with an imperfect ordering of the terminal ethylenedithio groups, occurs at 116 K in the pyridine compound. Note that no disorder is observed at low temperature for the benzonitrile phase.[3] This suggests that the difference of ordering of the BEDT-TTF end-groups is driven by the included molecules and causes the difference of physical properties.

These selected contributions have, to some extent, addressed the key interfacial chemistry issues raised here, with an emphasis on the steric demand of the neutral guests, disorder effects on the neutral molecule site, or the relevance of the interactions between the disordered ethylenedithio end groups and the mixed anion–solvent sublattice topology to the occurrence of metal-to-insulator phase transitions.

The opportunity is offered herein to focus on an homogeneous series of pseudopolymorphs that will be analyzed with the objective of tackling the difficult task of evaluating and understanding how the neutral guest molecules affect the very nature of the organic–inorganic interface. By giving an in-depth picture of how the crystal and electronic structures of prototypical phases of these series are related, we will be able to construct a coherent and comprehensive interfacial structure–activity–collective-transport-properties relationship.

Results and Discussion

Synthesis: All compounds were grown by electrocrystallization[4] and formed high-quality single crystals. The electrocrystallization experiments were conducted in acetonitrile containing 20% (by volume) of the guest molecule, with the exception of the water phases which were grown from a DMF/CH$_2$Cl$_2$ (1:1) solution containing only trace amounts of water. Guest molecules compete favorably with acetonitrile for inclusion into the crystal lattice, and it is likely that the methodology can be extended to the incorporation of many other neutral molecular guests. Note, however, that molecules such as methanol, dimethylformamide, (±)-alanine, and toluene resisted incorporation; this resulted in the synthesis of either β''-(BEDT-TTF)$_4$·(CH$_3$CN)·[Re$_6$S$_6$Cl$_8$] (no crystal at all) or the fully oxidized monoclinic and triclinic polymorphs,[5] (BEDT-TTF)$_2$[Re$_6$S$_6$Cl$_8$]. Altogether, 21 compounds were prepared and formulated by resolution of their crystal structures (Tables 1–5) as:

1: β''-(BEDT-TTF)$_4$·(H$_2$O)$_2$·[Re$_6$S$_6$Cl$_8$]
2: β''-(BEDT-TTF)$_4$·(H$_2$O)$_2$·[Re$_6$Se$_6$Cl$_8$]
3: β''-(BEDT-TTF)$_4$·(1,4-dioxane)·([Re$_6$S$_6$Cl$_8$]
4: β''-(BEDT-TTF)$_4$·(1,4-dioxane)·[Re$_6$Se$_6$Cl$_8$]
5: β''-(BEDT-TTF)$_4$·(1,4-dioxane)·[Re$_6$S$_5$OCl$_8$]
6: β''-(BEDT-TTF)$_4$·(THF)·[Re$_6$S$_6$Cl$_8$]
7: β''-(BEDT-TTF)$_4$·(THF)·[Re$_6$Se$_6$Cl$_8$]
8: β''-(BEDT-TTF)$_4$·(C$_2$H$_5$OH)·[Re$_6$S$_6$Cl$_8$]
9: β''-(BEDT-TTF)$_4$·(CCl$_4$)·([Re$_6$S$_6$Cl$_8$]
10: β''-(BEDT-TTF)$_4$·(CHCl$_3$)·[Re$_6$S$_6$Cl$_8$]
11: β''-(BEDT-TTF)$_4$·(CH$_2$ClI)·([Re$_6$S$_6$Cl$_8$]
12: β''-(BEDT-TTF)$_4$·(CH$_2$ClBr)·[Re$_6$S$_6$Cl$_8$]
13: β''-(BEDT-TTF)$_4$·(CH$_2$Cl$_2$)·[Re$_6$S$_6$Cl$_8$]
14: β''-(BEDT-TTF)$_4$·(CH$_2$OH-CH$_2$OH)·[Re$_6$S$_6$Cl$_8$]
15: β''-(BEDT-TTF)$_4$·(C$_5$H$_5$N)·[Re$_6$S$_6$Cl$_8$]
16: β''-(BEDT-TTF)$_4$·(CH$_3$COCH$_3$)·[Re$_6$S$_6$Cl$_8$]
17: β''-(BEDT-TTF)$_4$·(2-hydroxy-tetrahydrofuran)·[Re$_6$S$_6$Cl$_8$]
18: β''-(BEDT-TTF)$_4$·(CH$_3$CN)·([Re$_6$S$_6$Cl$_8$]
19: β''-(BEDT-TTF)$_4$·(CS$_2$)$_2$·[Re$_6$S$_6$Cl$_8$]
20: β''-(BEDT-TTF)$_4$·(CS$_2$)$_2$·[Re$_6$Se$_6$Cl$_8$]
21: β''-(BEDT-TTF)$_4$·(C$_6$H$_6$)·[Re$_6$S$_6$Cl$_8$]y

Compounds **2**, **4**, and **7** have already been reported in the hexarhenium selenium chloride cluster series[6] with the formulations, (BEDT-TTF)$_4$[Re$_6$Se$_5$Cl$_9$](DMF), (BEDT-TTF)$_4$[Re$_6$Se$_5$Cl$_9$](dioxane), and (BEDT-TTF)$_4$[Re$_6$Se$_5$Cl$_9$]-(THF), respectively. The identity and charge of the anion were at that time mistaken for [Re$_6$Se$_5$Cl$_9$]$^-$ instead of [Re$_6$Se$_6$Cl$_8$]$^{2-}$. Since then, it has been recognized that the former cluster monoanion transforms into the one-chalcogen-enriched dianion even at the moderate temperatures at which the electrocrystallization experiments were conducted.[7, 8] Besides, in this early work, the presence of water was overlooked in favor of a dimethylformamide molecule, the electrocrystallization solvent.[9] We now report that **1** and **2** are systematically obtained when electrocrystallization experiments are carried out in dimethylformamide containing only minute amounts of water.

Architecture and polymorphism: All phases adopt the same layered hybrid architecture in which single slabs of BEDT-TTF and inorganic cluster dianions alternate along the *b* axis direction (Figure 1). The BEDT-TTF slabs have β'' topology[10] (see Figure 8a below) with short molecular-axis-slipped dimers interacting with each other in the bond-over-ring mode. The cluster dianions are somewhat loosely arranged within the inorganic slab so as to leave enough room to incorporate one or, in the case of **1**, **2**, **19**, and **20**, two

  0947-6539/02/0817-3885 $ 20.00+.50/0

Table 1. Crystallographic data for **1**–**3** and **5**.

	1	**2**	**3**	**5**
Formula	$C_{40}H_{36}Cl_8Re_6S_{38}O_2$	$C_{40}H_{36}Cl_8Re_6S_{32}Se_6O_2$	$C_{44}H_{40}Cl_8Re_6S_{38}O_2$	$C_{44}H_{40}Cl_8Re_6S_{37}O_3$
M_r	3167.77	3445.14	3219.6	3203.5
Crystal size [mm]	$0.25 \times 0.20 \times 0.02$	$0.31 \times 0.23 \times 0.02$	$0.26 \times 0.25 \times 0.03$	$0.24 \times 0.21 \times 0.02$
Crystal system	triclinic	triclinic	triclinic	triclinic
Space group	$P\bar{1}$ (No. 2)	$P\bar{1}$ (No. 2)	$P\bar{1}$ (No. 2)	$P\bar{1}$ (No. 2)
a [Å]	9.0980(5)	9.082(2)	9.0908(14)	9.0506(13)
b [Å]	20.0584(13)	20.231(4)	20.027(2)	20.0358(28)
c [Å]	11.5664(7)	11.580(2)	11.6982(19)	11.7025(17)
α [°]	84.380(7)	84.33(3)	84.85(2)	84.607(17)
β [°]	101.405(6)	101.61(3)	101.32(3)	101.047(17)
γ [°]	79.318(7)	79.27(3)	78.495(16)	78.691(17)
V [Å^3]	2013.3(2)	2027.1(7)	2027.9(5)	2023.2(5)
Z	1	1	1	1
ρ [g cm^{-3}]	2.613	2.822	2.637	2.630
μ [mm^{-1}]	10.271	12.74	10.199	10.199
$F(000)$	1486	1590	1514	1506
T [K]	293	293	293	293
$2\theta_{max}$ [°]	55.76	47.84	55.96	55.94
Index range	$-11 < h < h11$	$-10 < h < h10$	$-12 < h < h11$	$-11 < h < h11$
	$-25 < hk < h25$	$-22 < hk < h22$	$-26 < hk < h26$	$-26 < hk < h26$
	$0 < hl < h15$	$0 < hl < h13$	$0 < hl < h15$	$0 < hl < h15$
Reflections measured	8836	16709	10228	24579
Observed reflections [$I > 2\sigma(I)$]	6082	3785	7155	6370
R_{int}	0.0523	0.0996	0.0417	0.0652
Parameters/restraints	422/0	429/0	443/0	443/0
R [$I > 2\sigma(I)$]	0.0280	0.0319	0.0342	0.0319
WR2 (all data)	0.0634	0.0665	0.0935	0.0624
$\Delta\rho$ (max/min) [eÅ^{-3}]	−0.961/1.803	−1.484/1.452	−2.391/2.191	−1.567/1.597

Table 2. Crystallographic data for **6** and **8**–**10**.

	6	**8**	**9**	**10**
Formula	$C_{44}H_{40}Cl_8Re_6S_{38}O$	$C_{42}H_{38}Cl_8Re_6S_{38}O$	$C_{41}H_{32}Cl_{12}Re_6S_{38}$	$C_{41}H_{33}Cl_{11}Re_6S_{38}$
M_r	3203.84	3177.8	3285.5	3251.1
Crystal size [mm]	$0.18 \times 0.14 \times 0.05$	$0.70 \times 0.33 \times 0.02$	$0.50 \times 0.35 \times 0.04$	$0.30 \times 0.16 \times 0.08$
Crystal system	triclinic	triclinic	triclinic	triclinic
Space group	$P\bar{1}$ (No. 2)	$P\bar{1}$ (No. 2)	$P\bar{1}$ (No. 2)	$P\bar{1}$ (No. 2)
a [Å]	9.0992(9)	9.0665(9)	9.1637(8)	9.1099(7)
b [Å]	20.0692(16)	20.070(4)	20.1127(19)	20.1141(18)
c [Å]	11.6444(12)	11.5471(12)	11.6256(11)	11.5609(9)
α [°]	84.693(11)	83.883(13)	85.030(11)	84.332(10)
β [°]	101.707(11)	101.175(12)	100.894(11)	101.066(9)
γ [°]	79.078(10)	79.670(13)	78.540(11)	78.978(10)
V [Å^3]	2025.4(3)	2006.1(4)	2044.9(3)	2020.4(3)
Z	1	1	1	1
ρ [g cm^{-3}]	2.627	2.630	2.668	2.672
μ [mm^{-1}]	10.21	10.31	10.24	10.33
$F(000)$	1506	1492	1540	1524
T [K]	293	293	293	293
$2\theta_{max}$ [°]	55.84	51.68	51.80	51.94
Index range	$-11 < h < h11$	$-10 < h < h10$	$-10 < h < h10$	$-10 < h < h10$
	$-24 < hk < h24$	$-24 < hk < h24$	$-24 < hk < h24$	$-24 < hk < h24$
	$0 < hl < h15$	$0 < hl < h14$	$0 < hl < h14$	$0 < hl < h14$
Reflections measured	8959	7114	7282	7385
Observed reflections [$I > 2\sigma(I)$]	5830	5928	6233	5806
R_{int}	0.0681	0.0875	0.0341	0.0408
Parameters/restraints	446/0	417/3	460/0	443/0
R [$I > 2\sigma(I)$]	0.0441	0.0317	0.0274	0.0264
wR2 (all data)	0.1022	0.0827	0.0724	0.0617
$\Delta\rho$ (max/min) [eÅ^{-3}]	−3.144/2.424	−2.099/1.666	−1.532/0.883	−1.574/1.238

neutral molecules within the hybrid host structure centrosymmetric cavity, which is delineated by four cluster anions and six BEDT-TTF molecules, as shown in Figure 1, as well as in a set of detailed representations in Figure 2.

It is important to discriminate within the series of 21 compounds between those (Tables 1–5) with the longest b axes, that is, in the range 19.930(2) to 20.311(2) Å, and those with the smallest b axes—in the range 17.926(2) to

0947-6539/02/0817-3886 $ 20.00+.50/0 *Chem. Eur. J.* **2002**, *8*, No. 17

Table 3. Crystallographic data for **11**–**14**.

	11	**12**	**13**	**14**
Formula	$C_{41}H_{34}Cl_9IRe_6S_{38}$	$C_{41}H_{34}BrCl_9Re_6S_{38}$	$C_{41}H_{34}Cl_{10}Re_6S_{38}$	$C_{42}H_{38}Cl_8O_2Re_6S_{38}$
M_r	3308.1	3261.12	3216.66	3193.8
Crystal size [mm]	0.35 × 0.22 × 0.04	0.64 × 0.26 × 0.02	0.30 × 0.20 × 0.02	0.30 × 0.12 × 0.04
Crystal system	triclinic	triclinic	triclinic	triclinic
Space group	$P\bar{1}$ (No. 2)	$P\bar{1}$ (No. 2)	$P\bar{1}$ (No. 2)	$P\bar{1}$ (No. 2)
a [Å]	9.1038(8)	9.0908(11)	9.0912(8)	9.0249(9)
b [Å]	20.027(2)	20.064(3)	20.0661(17)	20.014(2)
c [Å]	11.6206(10)	11.5752(16)	11.5683(10)	11.4942(12)
α [°]	84.633(11)	84.426(17)	84.299(10)	83.911(13)
β [°]	101.614(10)	101.450(15)	101.429(10)	100.960(12)
γ [°]	79.039(11)	79.326(16)	79.406(10)	79.637(13)
V [Å^3]	2018.2(3)	2013.7(5)	2013.0(3)	1983.8(4)
Z	1	1	1	1
ρ [g cm^{-3}]	2.722	2.689	2.654	2.673
μ [mm^{-1}]	10.66	10.797	10.337	10.425
F(000)	1544	1526	1508	1500
T [K]	293	293	293	293
$2\theta_{max}$ [°]	51.84	51.74	51.94	56.10
Index range	$-10 < h < 10$	$-10 < h < 10$	$-11 < h < 10$	$-11 < h < 11$
	$-24 < k < 24$	$-24 < k < 24$	$-24 < k < 24$	$-26 < k < 26$
	$0 < l < 14$	$0 < l < 14$	$0 < l < 14$	$0 < l < 15$
Reflections measured	7321	7116	7341	8861
Observed reflections [$I > 2\sigma(I)$]	5896	5190	5893	4826
R_{int}	0.0379	0.0125	0.0436	0.1114
Parameters/restraints	428/0	443/3	442/3	427/3
R [$I > 2\sigma(I)$]	0.0276	0.0497	0.0232	0.0463
wR2 (all data)	0.0609	0.1421	0.0525	0.1092
$\Delta\rho$ (max/min) [eÅ^{-3}]	−2.059/3.847	−3.461/2.075	−1.157/1.065	−2.111/3.622

Table 4. Crystallographic data for **15**–**18**.

	15	**16**	**17**	**18**
Formula	$C_{45}H_{37}Cl_8NRe_6S_{38}$	$C_{43}H_{38}Cl_8ORe_6S_{38}$	$C_{44}H_{39}Cl_8O_2Re_6S_{38}$	$C_{42}H_{35}Cl_8NRe_6S_{38}$
M_r	3210.84	3189.81	3231.83	3172.79
Crystal size [mm]	0.20 × 0.10 × 0.03	0.20 × 0.10 × 0.03	0.50 × 0.30 × 0.03	0.30 × 0.25 × 0.02
Crystal system	triclinic	triclinic	triclinic	triclinic
Space group	$P\bar{1}$ (No. 2)	$P\bar{1}$ (No. 2)	$P\bar{1}$ (No. 2)	$P\bar{1}$ (No. 2)
a [Å]	9.1193(9)	9.0965(7)	8.9528(10)	10.1817(9)
b [Å]	19.930(2)	20.1066(15)	20.016(3)	17.9265(18)
c [Å]	11.6638(11)	11.5884(9)	11.5307(13)	12.0806(11)
α [°]	84.862(12)	84.328(9)	84.926(14)	79.216(11)
β [°]	102.160(12)	101.415(10)	101.044(13)	109.749(10)
γ [°]	78.883(12)	79.183(9)	78.584(14)	86.100(11)
V [Å^3]	2014.6(3)	2020.2(3)	1970.6(4)	2018.0(3)
Z	1	1	1	1
ρ [g cm^{-3}]	2.647	2.622	2.712	2.611
μ [mm^{-1}]	10.265	10.236	10.496	10.246
F(000)	1508	1498	1513	1488
T [K]	293	293	293	293
$2\theta_{max}$ [°]	56.16	52.04	51.86	51.90
Index range	$-12 < h < 11$	$-11 < h < 10$	$-10 < h < 10$	$-12 < h < 11$
	$-25 < k < 26$	$-24 < k < 24$	$-24 < k < 24$	$-21 < k < 22$
	$0 < l < 14$	$0 < l < 14$	$0 < l < 14$	$0 < l < 14$
Reflections measured	9007	7281	7137	7210
Observed reflections [$I > 2\sigma(I)$]	5331	5392	4877	5445
R_{int}	0.0770	0.0423	0.0579	0.0373
Parameters/restraints	443/0	445/24	443/4	451/9
R [$I > 2\sigma(I)$]	0.0341	0.0367	0.0298	0.0235
wR2 (all data)	0.0706	0.0836	0.0654	0.0423
$\Delta\rho$ (max/min) [eÅ^{-3}]	−1.360/1.735	−1.732/1.925	−1.760/2.047	−0.534/0.609

19.236(3) Å. As shown in Figure 3, larger b axes are associated with a smaller, quarter of a molecule shift between $(BEDT\text{-}TTF)_2$ dimers within the slab, while a short b axis corresponds to a half interdimer molecular shift.

Compounds **1**–**17** belong to the long b-axis series and are defined as a first set of pseudoisomorphs.[11] Likewise, compounds **18**–**21** define a second set of pseudoisomorphs. Thus, pseudoisomorphism qualifies multicomponent (binary,

Table 5. Crystallographic data for **19**–**21**.

	19	**20**	**21**
Formula	$C_{42}H_{32}Cl_8Re_6S_{42}$	$C_{42}H_{32}Cl_8Re_6S_{36}Se_6$	$C_{46}H_{38}Cl_8Re_6S_{38}$
M_r	3284.0	3565.4	3209.84
Crystal size [mm]	0.40 × 0.30 × 0.08	0.40 × 0.25 × 0.05	0.46 × 0.40 × 0.08
Crystal system	triclinic	triclinic	triclinic
Space group	$P\bar{1}$ (No. 2)	$P\bar{1}$ (No. 2)	$P\bar{1}$ (No. 2)
a [Å]	10.331(1)	10.229(1)	10.0555(9)
b [Å]	19.236(3)	18.009(2)	18.0691(16)
c [Å]	11.477(1)	12.357(1)	12.4746(12)
α [°]	73.15(1)	79.38(1)	88.402(11)
β [°]	74.60(1)	110.20(1)	109.540(10)
γ [°]	76.58(2)	85.95(1)	75.184(11)
V [Å^3]	2074.5(7)	2077.4(6)	2048.9(3)
Z	1	1	1
ρ [g cm^{-3}]	2.629	2.850	2.601
μ [mm^{-1}]	10.069	12.532	10.093
F(000)	1542	1650	1508
T [K]	293	293	293
$2\theta_{max}$ [°]	55.78	51.82	51.86
Index range	$-12 < h < h13$	$-12 < h < h11$	$-12 < h < h11$
	$-23 < hk < h25$	$-21 < hk < h22$	$-22 < hk < h22$
	$0 < hl < h15$	$0 < hl < h15$	$0 < hl < h15$
Reflections measured	6474	7523	7428
Observed reflections [$I > 2\sigma(I)$]	5420	5888	6310
R_{int}	0.0496	0.0392	0.0588
Parameters/restraints	442/0	446/0	452/0
R [$I > 2\sigma(I)$]	0.0439	0.0329	0.0366
wR2 (all data)	0.1128	0.0884	0.0903
$\Delta\rho$ (max/min) [eÅ^{-3}]	−2.147/4.370	−1.718/1.625	−2.841/3.794

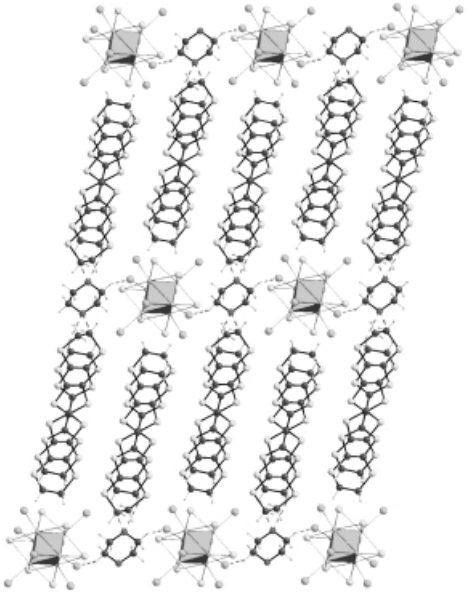

Figure 1. The common, layered hybrid architecture for all pseudopolymorphs, illustrated here for β''-(BEDT-TTF)$_4$·(1,4-dioxane)·[$Re_6S_6Cl_8$], **3**.

ternary) molecular solids whose host structures are strictly identical and that differ only by the nature of the incorporated guest. Then, **1**–**17** and **18**–**21** are in turn defined as pseudopolymorphs since the topology of their β'' slabs are different. Therefore, we will refer to the two sets of pseudopolymorphs by qualifying the corresponding phases by their inter-dimer β''(¼) and β''(½) topologies, as in Figure 3.

Interfacial chemistry

Steric demand of the guest on the cavity size: The steric demands of the incorporated molecules and the subsequent flexibility of their receptor host cavities are expressed through an increase in the unit cell volumes and the volumes estimated for the individual guest molecules (Figure 4). The latter are calculated as being 75% of the molar volume in the liquid state.[12] The ability of the neutral guest site surroundings to be molded by the cavity-forming process can be associated with the flexibility of the terminal ethylenedithio groups of the BEDT-TTF molecules[13] and the inherent, somewhat loose packing of the inorganic cluster anions within the slab; this has been exemplified recently for β-(BDT-TTP)$_6$[$Re_6S_6Cl_8$]·($CHCl_2$-CH_2Cl)$_2$.[14]

Moreover, the significant dispersity of the distribution of the data points in Figure 4 and the indication that the unit-cell volumes increase only half as much as the estimated volumes of the guests suggest that each molecular guest is defined by its own particular set of intermolecular weak interactions, and that the later are mostly attractive in nature. Now, if one focuses in Figure 4 on the four compounds **10**–**13**, a consistent set of chemically similar guests, the four data points for $CHCl_3$, CH_2ClI, CH_2ClBr, and CH_2Cl_2, are found neatly aligned on the ½ slope; this exemplifies the key influence of chemical nature of the guest.

How the guest incarceration perturbs the interfacial hydrogen bond network: A salient common feature of all 17 pseudoisomorphs β''(¼) is the persistent, robust network of C-H···Cl-μ-Re hydrogen bonds (Figure 2) which associates the ethylenedithio ends of the BEDT-TTF molecules with the apical,

  0947-6539/02/0817-3888 $ 20.00+.50/0 *Chem. Eur. J.* **2002**, *8*, No. 17

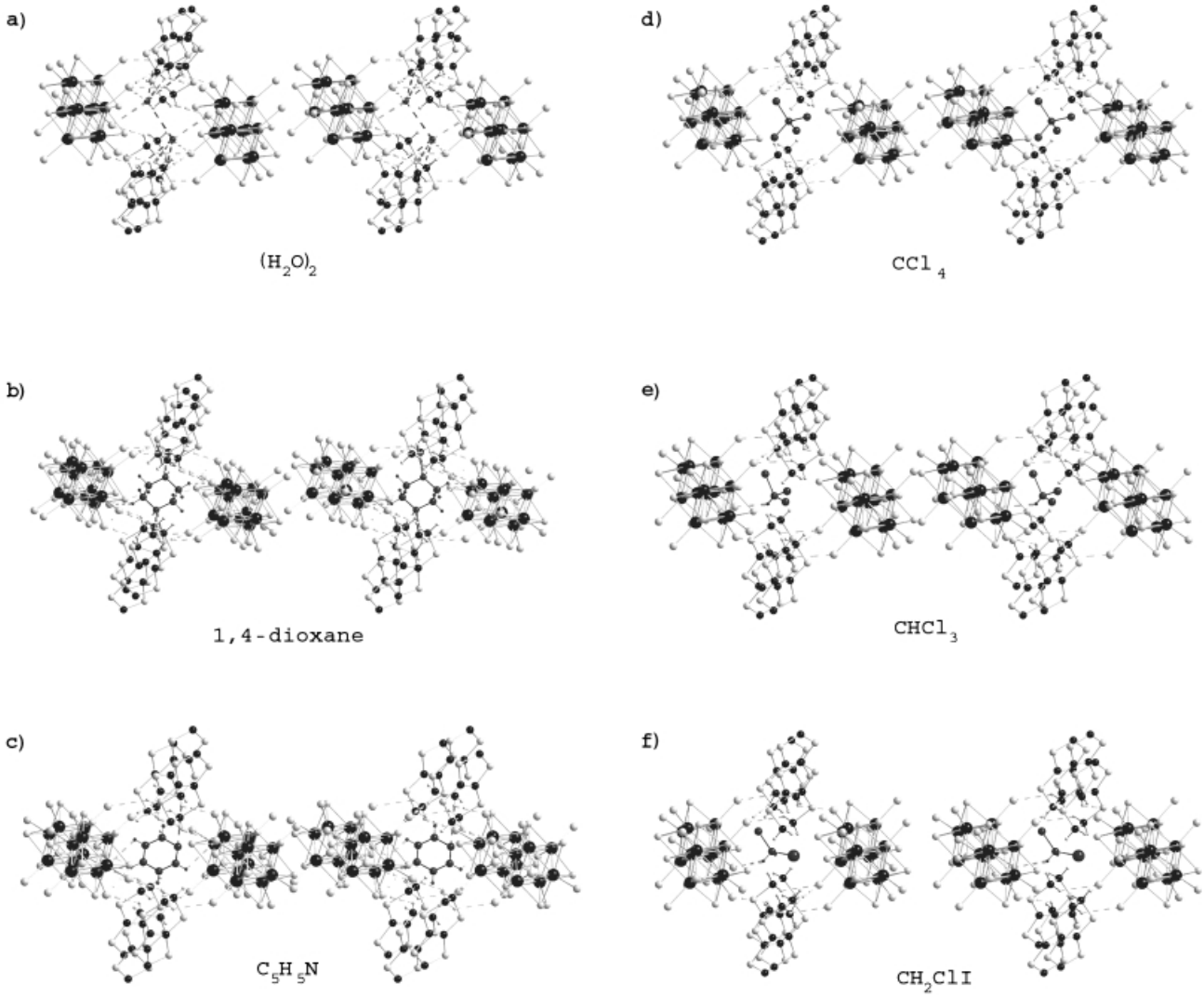

Figure 2. Stereoviews exemplifying interfacial intermolecular interactions in a) **1**, b) **3**, c) **15**, d) **9**, e) **10**, and f) **11**. The following interfacial hydrogen bonds: $(C–H)_{BEDT\text{-}TTF}\cdots$ guest; $(C\text{-}H)_{BEDT\text{-}TTF}\cdots$ Cl-μ-Re; and guest $\cdots$ Cl-μ-Re are represented by dashed lines. Relevant bond distances and bond angles are given in Table 6.

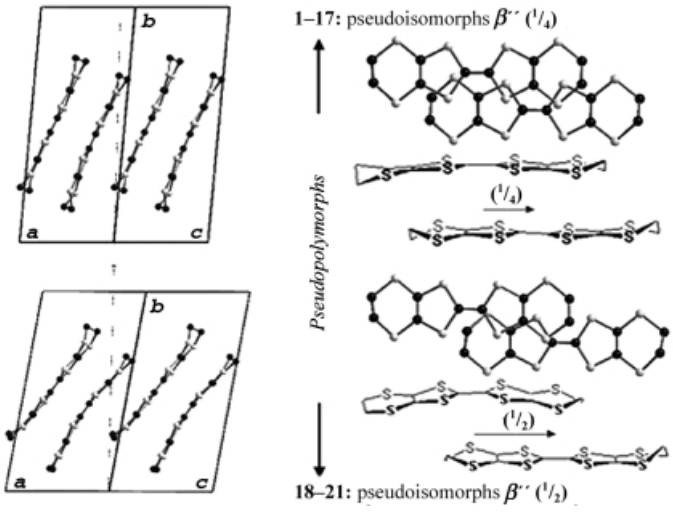

Figure 3. Illustration of the partition of the whole pseudopolymorph series into the two sub-sets of pseudoisomorphs. Note the strikingly different patterns of interdimer overlap defining the $\beta''(1/4)$ and $\beta''(1/2)$ topologies and their manifestation on the relative *b*-axis magnitudes.

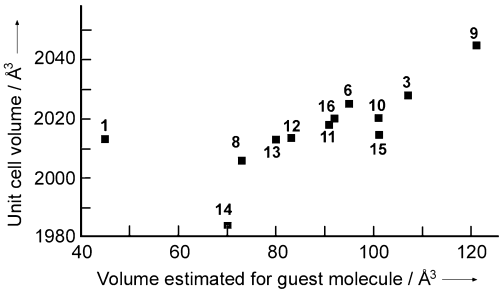

Figure 4. Correlation between pseudopolymorph unit-cell volumes and guest-molecule estimated volumes.

μ-Cl ligands of the inorganic cluster anions, thereby qualifying the hydrogen-bond-acceptor character of these halogen atoms, which are activated by complexation to the metal-cluster core.[15] Remarkably, the topology and distribution of these weak hydrogen bonds,[15] shown in Figure 2, are transferred throughout the series regardless of the nature of the guest molecule, and are likely to be significant in the

construction of the organic–inorganic interface during crystal growth. This network is taken as one manifestation of the isomorphic character of the $\beta''(¼)$ set, revealed here by virtue of the availability of this consistent set of data throughout the series. By an in-depth analysis of the interfacial intermolecular bonding within six particular $\beta''(¼)$ phases (Figure 2), namely **1**, **3**, **9**–**11**, and **15**, we shall decipher the whole interfacial hydrogen bond pattern—that is, the former array of C-H···Cl-μ-Re hydrogen bonds, eventually supplemented by the set of hydrogen bonds involving the neutral guest molecule—according to its hydrogen bond donor/acceptor (HBDA) ability. The first five structures now analyzed are those pseudoisomorphs in which the guest molecule only experiences an orientational disorder inherent to the presence of a center of symmetry in the cavity. In particular, no additional positional disorder occurs, as seen for example for **6** where two carbon atoms of the C_4H_8O ring statistically occupy two positions each of which is in turn doubled by the inversion center. In addition, all non-hydrogen atoms for **1**, **3**, **9**–**11**, and **15** were successfully refined with satisfactory anisotropic thermal parameters.

***β″(¼)* $(H_2O)_2$, 1**: The two water molecules are far apart (Figure 2a) (compare the oxygen–oxygen separation of 3.545(1) Å to that in ice of 2.76 Å), and provide (Table 6) three HO-H···Cl-μ-Re hydrogen bonds to the cluster anions and accept three C-H···OH_2 hydrogen bonds from the BEDT-TTF hydrogen-bond-donor molecules. Thus, a set of 3+3 weak hydrogen bonds per water molecule takes over and prevents the formation of a strong HO-H···OH_2 bond. Besides, the former set of intracavity hydrogen bonds are longer than the $(C\text{-}H)_{BEDT\text{-}TTF}$···Cl-$\mu$-Re hydrogen bonds involved in the host framework.

***β″(¼)* (1,4-dioxane), 3**: One salient feature stands out, that is (Figure 2b), the dioxane molecule primarily acts as an hydrogen bond acceptor vis-à-vis BEDT-TTF via three C-H···O hydrogen bonds,[16] one of which, $(C\text{-}H)_{BEDT\text{-}TTF\text{-}A}$···O, is as short as 3.296(3) Å (Table 6). In addition, the cluster anion terminal μ-chloride atoms accept hydrogen bonds equally from the C–H donors of BEDT-TTF and 1,4-dioxane.

***β″(¼)* (CCl_4), 9** (Figure 2d): The tetrachloromethane guest molecule neither accepts nor gives any hydrogen bond, an

Table 6. Interfacial hydrogen bond distances [Å] and angles [°] in **1**, **3**, **9**, **10, 11** and **15**.

1 (Figure 2a)	**3** (Figure 2b)	**9** (Figure 2c)	**10** (Figure 2d)	**11** (Figure 2e)	**15** (Figure 2f)
(C-H)···Cl-μ-Re involving BEDT-TTF/A	(C-H)···Cl-μ-Re involving BEDT-TTF/A	(C-H)···Cl-μ-Re involving BEDT-TTF/A	(C-H)···Cl-μ-Re involving BEDT-TTF/A	(C-H)···Cl-μ-Re involving BEDT-TTF/A	(C-H)···Cl-μ-Re involving BEDT-TTF/A
3.421(1)	3.410(5)	3.424(2)	3.370(2)	3.363(2)	3.365(3)
122.02(0)	120.33(5)	124.92(4)	124.78(5)	119.89(4)	121.39(8)
3.472(1)	3.419(4)	3.528(2)	3.565(2)	3.458(2)	3.405(3)
117.07	115.34(5)s	116.74(5)	116.65(5)	115.68(5)	118.88(8)
3.490(2)	3.527(7)	3.585(3)	3.496(3)	3.491(3)	3.486(4)
129.87(0)	130.77(5)	132.32(4)	128.98(4)	130.11(4)	133.96(7)
3.736(1)	3.795(5)	3.807(2)	3.756(2)	3.761(2)	3.781(3)
151.51(1)	148.87(6)	151.59(5)	153.41(6)	143.69(1)	150.33(9)
3.834(2)	3.769(6)	3.763(3)	3.789(3)	3.777(3)	3.746(4)
176.40(1)	173.73(10)	174.21(4)	176.53(4)	174.98(4)	175.35(9)
(C-H)···Cl-μ-Re involving BEDT-TTF/B	(C-H)···Cl-μ-Re involving BEDT-TTF/B	(C-H)···Cl-μ-Re involving BEDT-TTF/B	(C-H)···Cl-μ-Re involving BEDT-TTF/B	(C-H)···Cl-μ-Re involving BEDT-TTF/B	(C-H)···Cl-μ-Re involving BEDT-TTF/B
3.628(5)	3.651(3)	3.637(1)	3.643(1)	3.634(1)	3.600(2)
136.31(0)	134.44(4)	132.97(4)	137.18(4)	135.32(4)	130.42(7)
3.720(1)	3.698(5)	3.819(6)	3.796(2)	3.698(2)	3.680(3)
132.41(0)	129.08(4)	131.92(4)	132.55(5)	131.06(4)	129.87(7)
3.844(1)	3.751(6)	3.793(3)	3.757(2)	3.854(2)	3.781(3)
150.91(1)	155.92(6)	160.63(5)	148.82(5)	150.68(5)	150.33(9)
3.864(2)	3.954(4)	3.867(5)	3.896(3)	3.833(3)	3.940(3)
159.59(1)	153.93(6)	151.72(5)	165.99(5)	161.14(6)	152.05(8)
Re-μ-Cl···H-OH_2	Re-μ-Cl···H-C	–	Re-μ-Cl···H-CCl_3	Re-μ-Cl···H-C	Re-μ-Cl···H-C
3.711(1)	3.515(5)		3.579(2)	3.545(2)	3.434(2)
	140.37(6)		118.77(10)	110.42(10)	118.33(9)
3.937(1)	3.527(4)				3.554(3)
	108.56(7)				113.11(10)
3.969(1)	3.572(4)				3.665(2)
	116.34(6)				125.38(9)
	3.776(7)				3.720(4)
	134.72(6)				151.87(9)
H_2O···H-C	O···H-C	–	–	–	N···H-C
3.506(1) (B)	3.296(3) (A)				3.646(2) (A)
116.61(1)	134.67(5)				135.11(8)
3.622(8) (A)	3.468(2) (A)				
139.98(1)	121.30(5)				
3.898(1) (A)	3.487(3) (B)				
123.28(1)	140.95(5)				

0947-6539/02/0817-3890 $ 20.00+.50/0 *Chem. Eur. J.* **2002**, *8*, No. 17

observation consistent with the demonstration by Desiraju that chlorine atoms linked to a carbon atom have no hydrogen-bond-acceptor capacity.[15, 17] Therefore, CCl_4 is engaged in van der Waals interactions only, and will essentially impose steric constraints at the interface.

***β″*(¼) ($CHCl_3$)**, **10**: The single, neat Cl_3C-H ··· Cl-μ-Re hydrogen bond revealed in Figure 2e appears as anticipated, in agreement with the acidic character of the chloroform hydrogen atom. Thus, in comparison with **9**, the simple fact of changing the chemical nature of the guest induces i) a typical guest-fit pattern consistent with the chemical modification as well as ii) the offset of the data point for **9** in Figure 4.

***β″*(¼) (CH_2ClI)**, **11** (Figure 2f): The host cation–anion intermolecular interactions are identical for the $CHCl_3$ and CH_2ClI solvates. It is significant that essentially all interfacial hydrogen bonds are shorter in CH_2ClI than the corresponding ones in $CHCl_3$, **10** (Table 6); this demonstrates that the larger $CHCl_3$ molecule increases the cation–anion separation within the host framework. Note also, that only one out of the two hydrogen atoms of the guest molecule sees its hydrogen bond demand satisfied by one IClHC-H ··· Cl-μ-Re hydrogen bond, similar to, albeit shorter than, the corresponding one in **10**.

***β″*(¼) (C_5H_4N)**, **15** (Figure 2c): Just like 1,4-dioxane, pyridine is both a hydrogen bond donor and acceptor molecule. Most hydrogen bonds, notably $(C\text{-}H)_{BEDT\text{-}TTF}$ ··· Cl-μ-Re and $(C\text{-}H)_{guest}$ ··· Cl-μ-Re, appear shorter than for **3** (Table 6). Remarkably though, the C-H ··· N bond distance (3.646(2) Å) is significantly longer than the corresponding C-H ··· O in **3** (3.296(3) Å); this is in keeping with the enhanced availability of the ether oxygen lone pairs.

As a conclusion of this analysis it appears that the guest molecules are engaged in hydrogen bond interactions similar in nature and strength to the robust $(C\text{-}H)_{BEDT\text{-}TTF}$ ··· Cl-μ-Re donor-anion interactions. Therefore, significant modifications of the set of $(C\text{-}H)_{BEDT\text{-}TTF}$ ··· Cl-μ-Re are observed for all five pseudoisomorphs (Table 6). Thus, the most striking manifestation of a global, balanced reconstruction of the interfacial pattern of interactions upon guest incorporation is readily apparent in the lengthening of one $(C\text{-}H)_{BEDT\text{-}TTF}$ ··· Cl-μ-Re from 3.405(3) Å for **15** to 3.565(2) Å for **10**, or of another from 3.486(4) Å for **15** to 3.585(3) Å for **9** (Table 6). This demonstrates the inherent cooperativity of the hydrogen-bond arrays at the organic–inorganic interface: changing the chemical activity and HBDA character from one guest molecule to another results in a small, balanced modification of an homogenous set of donor-anion and specific guest interfacial intermolecular interactions that affect the whole extended interface, even at large length scales.

A dynamic virtual cavity: The above study demonstrates that the shape, volume, and hydrogen-bond-donor–acceptor character of the guest molecules are important factors in the cavity-forming process. These factors are expressed by virtue of the adaptability, defined as a chemical activity, of a virtual receptor cavity. The concept of a dynamic virtual cavity is an uncommon and distinctive feature of such series of pseudopolymorphs, an expression of the dynamics of balanced intermolecular interactions at the organic–inorganic interface. The balance of hydrogen-bond strengths at the interface has been shown to be affected by, and even to be specific to, the nature of the guest molecule (Table 6). Each successful inclusion qualifies a thermodynamic equilibrium:

$$\text{cavity (free)} + x\,\text{guest} \rightarrow \text{cavity (guest)}_x \qquad K_{\text{incl}}(\text{guest})$$

$$\text{with } K_{\text{incl}}(\text{guest}) = \frac{\text{“}a\,[\text{cavity (guest)}_x]\text{”}}{\text{“}a\,\text{cavity (free)”} \times a\,(\text{guest})}$$

here *a* designates an activity. Although acetonitrile is used as the primary solvent, always in large excess of the putative guest molecule solution volume in the electrocrystallization experiments, the acetonitrile solvate **15** is only obtained for pure acetonitrile solutions. This suggests that encapsulation of the guest molecules during the electrocrystallization process occurs under thermodynamic control. It follows that acetonitrile molecules have less affinity for the virtual cavity than those molecules selectively included, hence $K_{\text{incl}}(\text{acetonitrile}) < K_{\text{incl}}(\text{included guest molecules})$. On the other hand, the preparation of a number of solvates such as dimethylformamide, methanol, alanine, and toluene has either failed or has resulted in the incorporation of acetonitrile. Thus, for these guest molecules, $K_{\text{incl}}(\text{acetonitrile}) > K_{\text{incl}}(\text{included guest molecules})$. Likewise, water molecules, however sparse they may be during the electrocrystallization experiments, have a stronger affinity for the virtual cavity than dimethylformamide, that is, $K_{\text{incl}}(\text{dimethylformamide}) < K_{\text{incl}}(\text{water})$. Consistently then, when experiments are conducted in rigorously dried dimethylformamide, a novel monoclinic phase is obtained;[9] this demonstrates that $K_{\text{incl}}(\text{dimethylformamide}) = 0$. Estimation of these constants would require a calculation of all weak intermolecular interactions at the interface, hydrogen bonds and van der Waals interactions alike, in a formalism which would embrace their inherent cooperativity at various, eventually large length scales.

Toward an enantiomeric molecular recognition? We have here a versatile, albeit selective, virtual cavity. Just how sensitive is the guest–cavity entity forming process to allow enantiomeric recognition along with crystallization at the vicinity of the electrode surface? As a first step in this direction, single crystals of **17** were successfully grown by using (±)-2-hydroxytetrahydrofuran. A precise refinement of the positions of the guest molecule within the cavity and an analysis of the Fourier difference maps provide evidence for a slight imbalance in favor of one position of the hydroxy group in the crystal, which would result in a 10% enantiomeric excess. Note, however, that the high electron density due the rhenium atoms of the anions precludes definitive conclusions.

Metallic character, Fermi surface topology, and metal–insulator phase transitions: All thirteen phases, **1**–**7**, **9**–**10**, **13, 15**, **17**, and **19**, for which the temperature dependence of the transport properties has been investigated, exhibit metallic

  0947-6539/02/0817-3891 $ 20.00+.50/0

character at room temperature (Figure 5 and Figure 11 in the Supporting Information). The water pseudoisomorphs **1** and **2** are the only two phases to remain metallic down to 4.2 K (Figure 5a). All other phases experience a more or less pronounced increase of their resistivity at low temperature. For **3** and **10**, which present sharper resistivity upturns (Figure 5b and c), the metallic state was restored down to 4.2 K by application of hydrostatic pressures of 15 and 8 kbar, respectively.

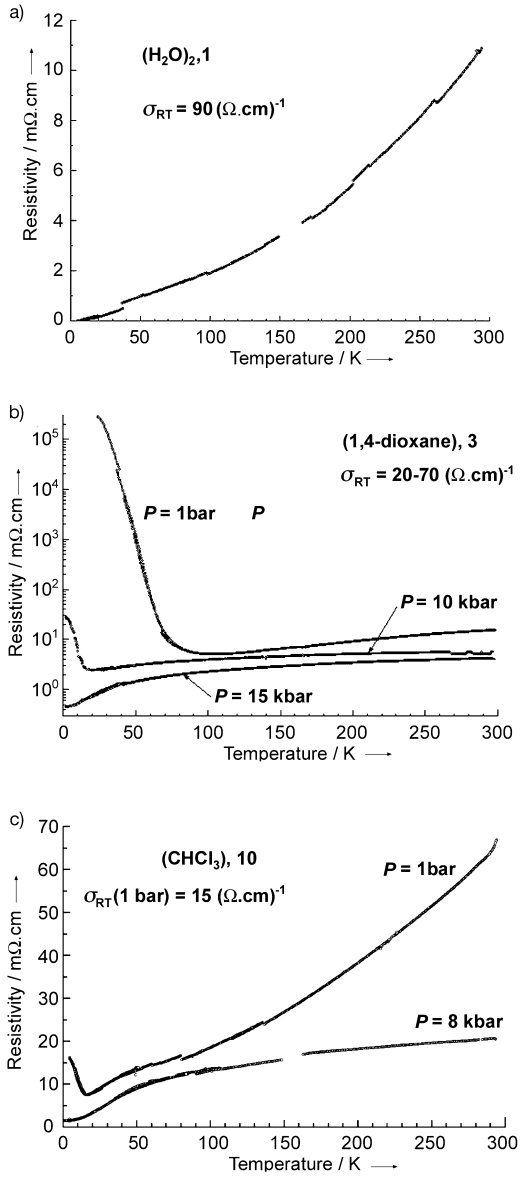

Figure 5. Temperature dependence of the resistivity measured by the four-point method for one single crystal of a) **1**, and at different pressures for b) **3** and c) **10;** the values of the room-temperature conductivities are indicated.

In order to analyze the correlation between the crystal structure and the transport properties of this set of phases we have performed tight-binding band structure calculations for many of these salts. Here we shall only report the results for **1**–**3** and **19**. This set of four salts should be representative of the different situations encountered in this family. Salts **1** and **2** contain the same solvent but different anions so that the donor–donor transfer integrals (and thus the details of the band structure and Fermi surface) can be different because donors and anions are connected through hydrogen bonds.[6] In contrast to **1** and **2**, which keep their metallic character down to very low temperature, **3** exhibits a sharp resistivity upturn. Finally, salt **19** belongs to a different set of pseudo-polymorphs, and this can also lead to differences in the band structure.

Band structure and Fermi surfaces: The calculated band structures near the Fermi level for the donor layers of **1** is reported in Figure 6a. There are four donors per repeat unit of the layer, so the four bands of Figure 6a are mainly built from

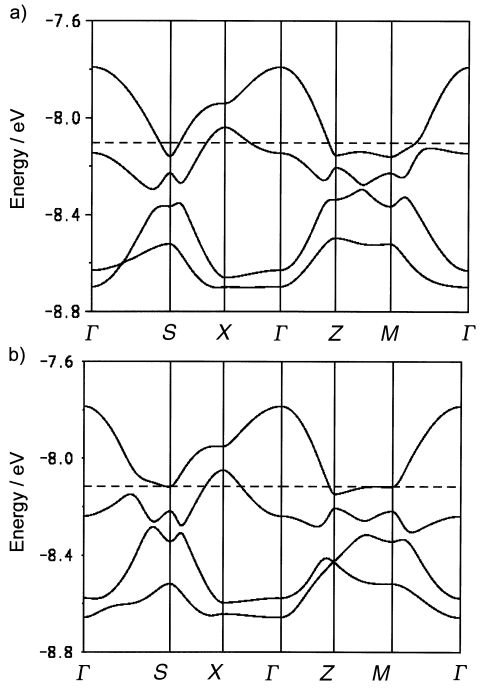

Figure 6. Calculated band structures for the donor layers of a) **1** and b) **19**. The dashed line refers to the Fermi level and $\Gamma=(0,0)$, $X=(a^*/2,0)$, $Z=(0,c^*/2)$, $M=(a^*/2,c^*/2)$ and $S=(-a^*/2,c^*/2)$.

the HOMO (highest occupied molecular orbital) of BEDT-TTF. The HOMO of the two different donors of the layers are quite similar in energy (i.e., the difference is usually within 0.1 eV) so that they strongly mix and lead to the quite dispersive bands of Figure 6a. According to the usual oxidation states, the average charge of the donors is $+0.5$ and consequently, there should be two holes in the bands of Figure 6a. With four HOMO bands and two holes, the salt could be either a semiconductor (if there is a band gap between the two upper HOMO bands) or a metal (if the two upper bands overlap). As shown in Figure 6a, the system is predicted to exhibit metallic behavior at room temperature in agreement with the resistivity measurements. The band structures calculated for the donor layers of **2** and **3** are very similar to that of Figure 6a and thus, the same conclusion applies.

0947-6539/02/0817-3892 $ 20.00+.50/0 *Chem. Eur. J.* **2002**, *8*, No. 17

The Fermi surfaces calculated for the donor layers of **1**, **2** and **3** are shown in Figure 7a–c, respectively. These Fermi surfaces can be described as having two contributions: i) a closed two-dimensional hole pocket centered at X, and ii) an open pseudo-one-dimensional electron pocket parallel to the a^* direction. However, the Fermi surfaces of Figure 7a–c can also be seen as a superposition of ellipses (with approximately the area of the Brillouin zone) if we disregard the band hybridization, that is, the creation of gaps at the regions where these ellipses superpose. This suggests that the systems with donor layers of the $\beta''(¼)$ topology should be described as 2D metals despite the presence of open lines in the Fermi surface.

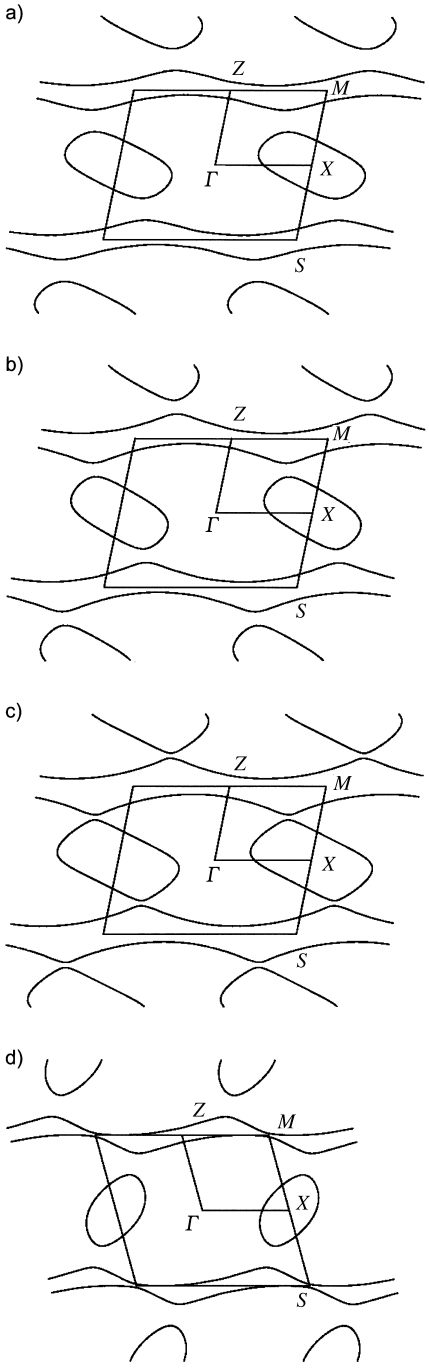

Figure 7. Calculated Fermi surfaces for the donor layers of a) **1**, b) **2**, c) **3**, and d) **19**. $\Gamma=(0,0)$, $X=(a^*/2,0)$, $Z=(0,c^*/2)$, $M=(a^*/2,c^*/2)$ and $S=(-a^*/2,c^*/2)$.

The main difference between the three Fermi surfaces of Figure 7 is that the gap between the hole and electron pockets increases from almost touching for **3** to being well separated in **1**. Can this fact be related to the difference in the resistivity versus temperature behavior between salt **3** and salts **1** and **2**? In principle, the loss of metallic behavior at low temperature could be due to three different mechanisms: i) the disappearance of the Fermi surface through a Fermi-surface-nesting mechanism that will lead to an additional modulation of the charge or spin density, ii) a small structural change suppressing the band overlap between the two upper HOMO bands without changing the size of the repeat unit of the layer, and iii) an electronic localization. The last possibility could be favored by the intrinsic disorder in some of these systems.[18] However, at least for **3**, the resistivity upturn is too sharp to be adequately explained by this kind of mechanism, and we believe that most likely it should have a structural origin. Note that mechanism (ii) does not require the appearance of a modulation as it is the case for mechanism (i). The only thing needed is some kind of structural change that slightly modifies some of the transfer integrals in such a way that the dispersion of the two upper bands decreases and they do not overlap any more. The elliptical nature of the Fermi surface does not allow for good nesting conditions, and thus the system appears to be unable to undergo a Fermi surface driven distortion (mechanism (i)) at low temperature. However, the overlap between the ellipses, and equally the overlap between the two upper bands, is so large that the structural change underlying mechanism (ii) should be too large, and we do not believe that it provides for an adequate rationalization. Thus, no clear explanation seems to emerge at this point. However we have yet to consider a key point in the discussion of the electronic structure of molecular metals: how stable are the Fermi surfaces of Figure 7 with respect to small changes in the donor···donor interactions?

Understanding the crystal and electronic structures relationship: In order to investigate the dependence of the shape of the Fermi surface on the intermolecular contacts, a simulation study with different values for the $t_{\text{HOMO-HOMO}}$ transfer integrals was performed. The repeat unit of the donor layers of all these systems contains four donor molecules (see Figure 8a): two of type A and two of type B. Each of the molecules is related to others of the same type by an inversion center. The HOMO energy of the two donors are -8.430 eV (A) and -8.454 eV (B) for **3**, -8.527 eV (A) and -8.481 eV (B) for **2**, and -8.432 eV (A) and -8.524 eV (B) for **1**. These values, as well as the almost identical central carbon–carbon bond lengths within the molecules, indicate that molecules A and B are crystallographically different but electronically essentially the same for **3**. However, for the systems containing water as a guest species the two molecules are electronically not as similar. This is more due to the ethylenedithio groups and the small geometrical changes induced by them than to the central carbon–carbon double bond, which remains practically identical in all these systems. This is an important observation whose implications will become clear later in our discussion

  0947-6539/02/0817-3893 $ 20.00+.50/0

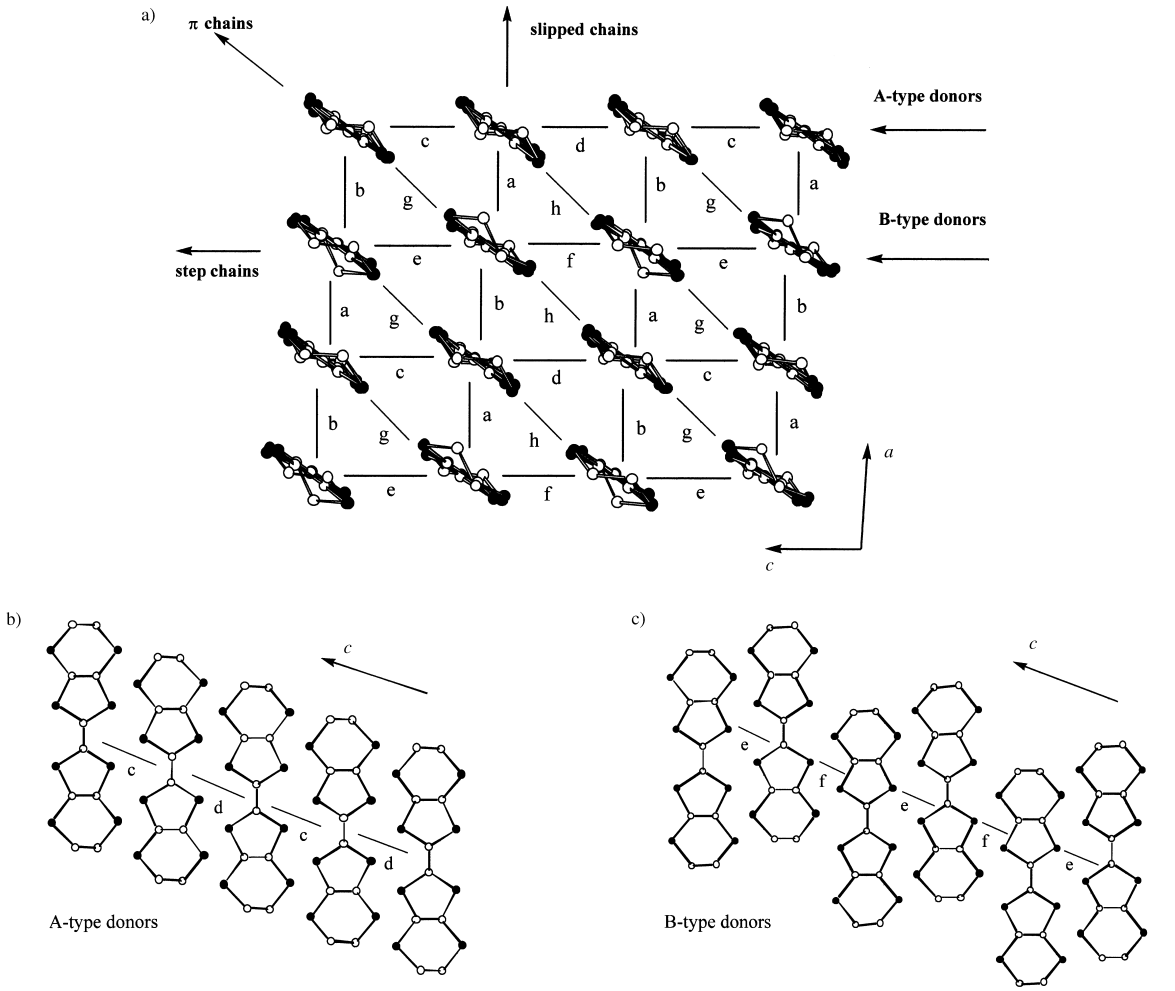

Figure 8. a) Schematic representation of the donor layers of systems **1**–**3** in which the different types of interactions and donors are labeled; b) step-chains of donors A in **1**–**3**, and c) step-chains of donors B in **1**–**3**.

The donor layers of these systems contain eight different types of donor···donor interactions (labeled a–h in Figure 8a). The calculated values of the $t_{HOMO\text{-}HOMO}$ transfer integrals for **1**–**3** are given in Table 7. The eight interactions are of three different types. The first group consists of the integrals a and b. Both of these interactions act in the *a* direction and are quite small. These two interactions are small due to the large separation between the mean planes of the BEDT-TTF molecules. The second group of interactions is those labeled c–f. The organic donor layers can be seen as a series of two different types of step-chains running in the *c* direction. The first is associated with A-type molecules through interactions c and d, whereas the second is associated with B-type molecules through interactions e and f. Whereas interactions c and d are very similar, interaction e is much larger than f in the three salts. Thus, from the viewpoint of the HOMO–HOMO interactions, the step-chain consisting of A molecules can be considered as uniform whereas the step-chain consisting of B molecules can be considered as strongly dimerized. As shown in Figure 8b and c, there are strong structural reasons underlying this fact. For instance, in **1** there are five S···S contacts shorter than 3.9 Å for interaction e but only two for interaction f. In contrast, the number of short S···S contacts is six and five for interactions c and d, respectively. The third group of interactions are those labeled g and h which act in the $(a+c)$ direction. These integrals are of intermediate strength because the HOMO–HOMO overlap is of the π type. The above classification of interactions allows us to describe the layers of donors as consisting of a series of parallel stacks of slipped donors along the *a* direction, as a series of step-chains along the *c* direction, or as a series of parallel chains of donors making lateral contacts along the $(a+c)$ direction. In the following, the three types of chains will be refereed to as slipped-chains, step-chains and π-chains.

Table 7. Calculated $t_{HOMO\text{-}HOMO}$ transfer integrals (meV) for the donor layers of **1**, **2**, and **3**.

Interaction[a]	**1**	**2**	**3**
a	– 65	– 48	– 45
b	– 46	– 30	– 22
c	191	194	195
d	200	199	189
e	224	221	230
f	113	109	120
g	– 81	– 71	– 68
h	– 85	– 79	– 64

[a] See Figure 8a for labeling.

0947-6539/02/0817-3894 $ 20.00+.50/0 *Chem. Eur. J.* **2002**, *8*, No. 17

The transfer integrals are very similar for the three phases **1**, **2**, and **3**. From the values in Table 7 it is clear that, as far as the HOMO–HOMO interactions are concerned, these layers should have a strong 1D character because of the large interactions c–f along the step-chains in the *c* direction. However, these chains are coupled in the (*a*+*c*) direction through the g–h interactions, and hence the material acquires a 2D character (Note that these interactions are not only larger but also very uniform in contrast to the alternation of the weaker interactions along the *a* direction. Both facts, weakness and alternation, cooperate in making the role of the last interactions quite small). The similar nature of the transfer integrals for the three phases explains why both the band shapes and overall band widths of these materials are almost identical, but does not explain why we find a larger separation of the closed and open parts of the Fermi surface for the compounds in which water is the guest molecule.

In order to tackle this problem, we carried out a series of numerical simulations of the electronic structure of these compounds by using initially the transfer integrals of phase **3** and identical HOMO energies for donors A and B.[19] The transfer integrals of each type (i.e., along the step-chains, along the π-chains and finally along the slipped-chains) were then changed individually or together within a given type into their values for **1** or **2**. We find this has practically no effect on the separation of closed and open portions of the Fermi surface: they always remained almost touching. We are then led to the conclusion that for the electron filling and the range of HOMO–HOMO interaction strengths of these systems there is no reason for the difference in the Fermi surfaces.

We next carried out simulations in which the transfer integrals were kept at their values for **3** but where the HOMO energies of donors A and B were changed. When the difference in HOMO energies was progressively changed from 0.0 (approximately the situation for **3**) to 0.10 eV (approximately the situation for **1**), we found that the separation of the two portions of the Fermi surface progressively increases regardless of which donor, A or B, possessed the lower HOMO. In fact, the Fermi surface simulated when the HOMO of donor B is 0.10 eV lower in energy is in excellent agreement with the real Fermi surface for **1**. Thus, from these simple numerical simulations, we may conclude that these materials are all essentially identical from the electronic standpoint, except for the fact that the difference in HOMO energies between the two donors controls the overlap between the two upper HOMO bands and thus, the separation between the closed and open portions of the Fermi surface.

It is possible to go a step further in the understanding of the electronic structure of these systems (and in general of any donor layer of the β'' type). The main aspects of their electronic structure can be understood on the basis of a very simple qualitative scheme.[10, 20] Let us first assume that the HOMO energies (α_i) are equivalent; this provides us with essentially four identical molecules in a unit cell. Thus, for the sake of simplicity we shall construct our model using a value of $\alpha = 0.0$ eV for all four molecules in the unit cell. We shall consider the variation in this parameter below. For further simplicity, we average transfer integrals of the same type, thus reducing the problem to one of only three transfer integrals:

$$t_1 = (t_g + t_h)/2$$

$$t_2 = (t_a + t_b)/2$$

$$t_3 = (t_c + t_d + t_e + t_f)/4$$

in which t_1, t_2 and t_3 are the transfer integrals along the π-chains, slipped-chains, and step-chains, respectively. We will take as the values of the transfer integrals those estimated from the actual ones in **3**: $t_1 = -0.066$ eV, $t_2 = -0.035$ eV, and $t_3 = 0.185$ eV. These assumptions allow us to reduce the complex band structure of the four-molecule unit cell down to a simple model for which one needs to solve only a one molecule, one orbital per unit cell band structure. This problem may be readily solved analytically and extended to the larger four-molecule unit cell by artificially doubling the unit cell in both the *a* and *c* directions to see how well it reproduces the band structure of the real system. The details of this approach will be given elsewhere,[20] but for the current purposes this allows us to see what factors govern the overall shape of the bands and then extract what effects the disruption from high symmetry has on the electronic structure of the donor layer. We summarize in Table 8 the energy levels and the correlation of the bands, with respect to the Brillouin zone of the four-molecule cell, which we obtained from the simple analytical treatment. We also depict this as a schematic band structure in Figure 9a.

Table 8. Summary of the results concerning the band levels at special *k* points from the model study.

k point	band	energy
Γ	*1*	$2(t_1 - t_2 - t_3)$
	2	$2(-t_1 + t_2 - t_3)$
	3	$2(t_1 + t_2 + t_3)$
	4	$2(-t_1 - t_2 + t_3)$
X	*1*	$-2t_3$
	2	$-2t_3$
	3	$2t_3$
	4	$2t_3$
Z	*1*	$-2t_2$
	2	$-2t_2$
	3	$2t_2$
	4	$2t_2$
S	*1*	$2t_1$
	2	$-2t_1$
	3	$2t_1$
	4	$-2t_1$
M	*1*	$-2t_1$
	2	$2t_1$
	3	$-2t_1$
	4	$2t_1$

Let us briefly examine this simple model to see how well it captures the flavor of the electronic structure of these systems. First consider the special point *Γ*. These energy levels provide the extreme limits of the band with the lowest energy orbital being *1* and the highest energy orbital being *4* (see Figure 9a and Table 8). The total bandwidth is related to $4(|t_1| + |t_3|) = 1.004$ eV, in good agreement with the calculated value of 0.91 eV. Most of the difference is due to mixing with lower energy orbitals, which occurs at the bottom of the HOMO bands, a factor not present in this simple model and which will slightly reduce the total bandwidth. Dispersion along the *Γ*-*X* direction involves the integrals acting with a component in the *a* direction (t_1, t_2). For the lower two bands these two integrals act against each other and thus cancel; this leads to relatively flat bands, whereas they work in an additive fashion for the upper two bands; this leads to a large

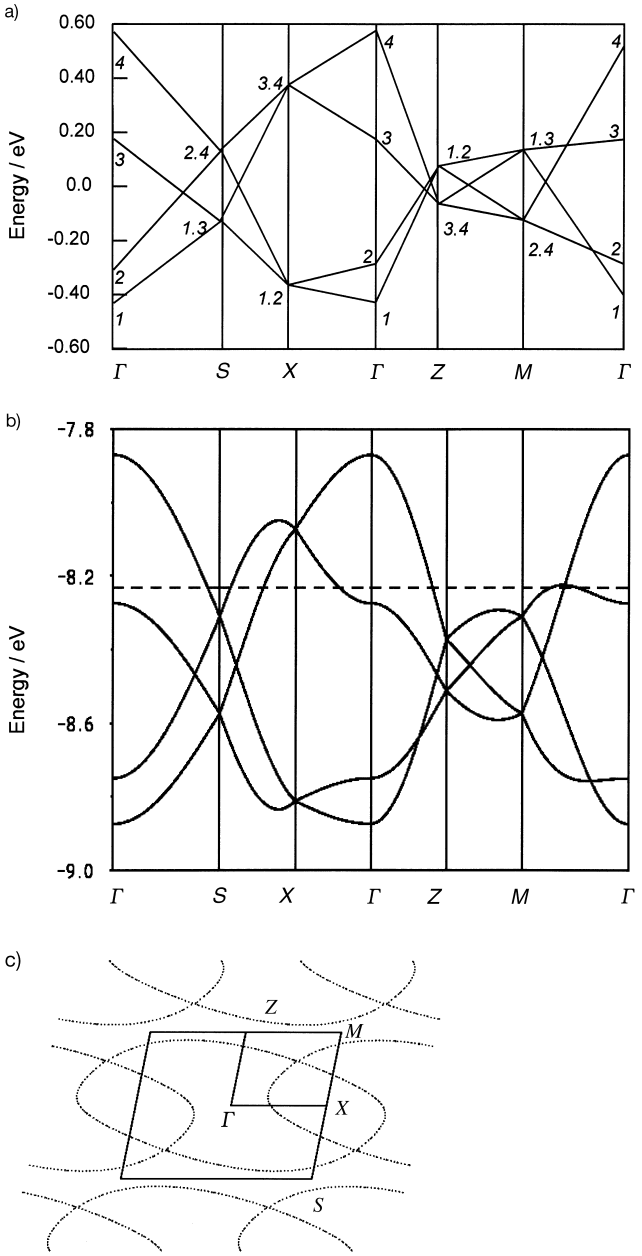

Figure 9. a) Schematic band structure obtained from simple analytical treatment. b) Simulated band structure from simple analytical treatment, and c) Fermi surface associated with the band structure of Figure 9b.

dispersion. In the Γ-Z direction, integrals t_2 and t_3 are involved. The fact that t_3 is much larger than t_2 leads to all four bands having significant dispersion in this direction. Similar arguments may be made for all directions in k space.

The overall picture obtained from the above description is that the upper two bands are 2D and account for the elliptical Fermi surface. However, the two dimensionality goes much deeper. All this model is, is a folded one-orbital band acting in two directions, that is, all the four HOMO bands are really just one 2D HOMO band with gaps opened at specific points in the Brillouin zone caused by the lower symmetry of the crystal structure. Before discussing the effects of the lattice topology on the HOMO bands, we consider the question of how well this simple folded one-orbital approach reproduces the actual bands and Fermi surface calculated for these materials. The simulated band structure and Fermi surface from this simple analytical model (the average transfer integrals and HOMO energy levels for **3** were used in this simulation) are presented in Figure 9b and c, respectively. The simple model does indeed reproduce the band structure from the full calculation very well. We also note that the simulated Fermi surface is found to resemble a distorted ellipse of area equal to the Brillouin zone, as well as that from the full calculation. Thus, we can conclude that, to a large degree, the distortion of the lattice from the ideal high symmetry situation is only a minor effect, and that the electronic structure retains a strong memory of the 2D one-orbital band.

It is now very easy to see how the actual band structures (like that of Figure 6a) can be understood on the basis of the ideal band structure (Figure 9a) when the details of the real lattice topology are taken into account. First, this process lowers the symmetries of all the bands and causes all of the crossings to become avoided crossings. Second, the degeneracies at X and Z are removed. At Z for example, it is the dissymmetry in the step-chain interactions (i.e., the dimerization in the B-type step-chains) that is the major contributor to the lifting of the degeneracies. At X, the major contributor to the lifting of the degeneracies is the smaller interactions, which are much more similar, and consequently the energy splitting is much smaller. At M, it is again the dissymmetry in the step-chain interactions that is the leading factor breaking the degeneracies. Most of the details of the band structure of any of these systems can thus be correlated with those of the crystal structure in a similar vein once the transfer integrals are calculated.

Finally, we must consider the effect of changing the energy of the two HOMOs, that is, going away from the simple one-orbital model. For relatively small (ca. 0.1 eV) differences, such as those we noted above for these salts, it is very simple to understand the consequences. These moderate differences in the HOMO energies will introduce an additional dissymmetry into the lattice, which will provide for an additional factor contributing to the lifting of the degeneracies of the two upper bands. In other words, as the energy difference between the two HOMOs increases, the two upper bands will overlap less, and the separation between the closed and open portions of the Fermi surface will increase. This explains the differences between the Fermi surfaces of Figure 7a, b and c.

Thus, we now have an in-depth picture of how the crystal and electronic structures of the layers are related. What remains to be seen is: how can we use this to help us understand the phase transition in **3**?

Origin of the metal-insulator transition in 3: We now turn to using this information in order to understand how changes in the $t_{\text{HOMO-HOMO}}$ transfer integrals of these systems (Table 7) can change the shape of the Fermi surface. To do this, consider the following observations. First, interactions c – f are strong and act only in the c direction (step-chains). Second, interactions a – b act purely in the a direction and are quite small. Third, it is interactions g and h that couple the step-chains and lead to the 2D character of the HOMO bands and

  0947-6539/02/0817-3896 $ 20.00+.50/0 *Chem. Eur. J.* **2002**, *8*, No. 17

Fermi surface. Hence one might expect that either an increase or decrease of interactions a–f by a reasonable amount will not change the dimensionality but that interactions g and h can. We note further that the topology of the lattice requires that both interactions g and h decrease simultaneously in order to achieve this.

Let us consider again the donor layers in **3** in which all molecules can be considered equivalent. The integrals a–f were varied (individually or for a given type of chain) by values of $\pm 20\,\%$, and it was found that the Fermi surface remained a series of overlapping ellipses. This is in contrast to the case of simultaneously decreasing interactions g and h, which has the effect of reducing the Fermi surface dimensionality to 1D. In the limit of g and h approaching zero, these contours become equivalent, and the Fermi surface may be nested by the vector $\boldsymbol{q} = 0.5\,c^*$. This change in transfer integrals leaves the lattice as a series of step-chains weakly coupled in the *a* direction. We illustrate this in Figure 10, where we plot the simulated Fermi surface as a function of the parameter γ which modulates the strength of the transfer integrals for interactions g and h (i.e., $t_g' = \gamma t_g$ and $t_h' = \gamma t_h$). Thus, it can be concluded that a Fermi surface nesting mechanism is a likely explanation for the metal–insulator transition in **3**, provided that the necessary structural requirements for decreasing those integrals are feasible. This kind of "assisted" (because it needs some structural change to conveniently modify the Fermi surface) or "hidden" (because it is not obvious from the room-temperature Fermi surface) nesting mechanism is thought to be at the origin of the metal–insulator transition in $(BEDT\text{-}TTF)_2ReO_4$.[21]

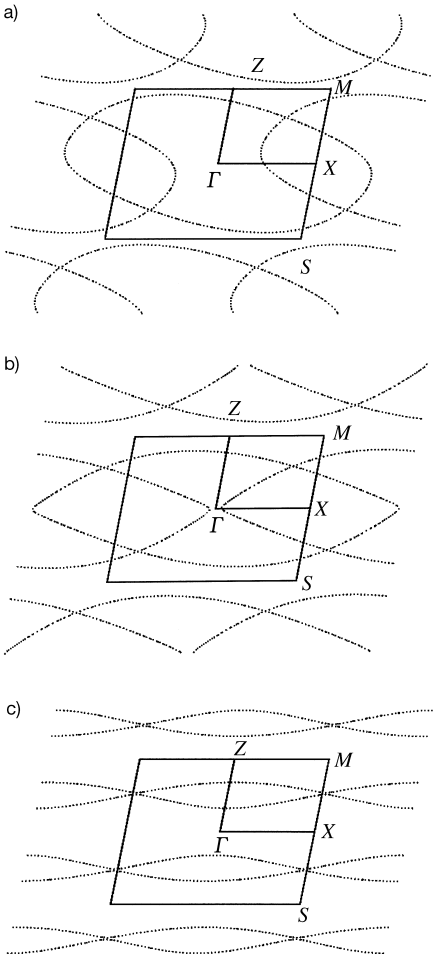

Figure 10. Simulated Fermi surfaces as a function of the parameter γ which modulates the strength of the transfer integrals for interactions g and h (i.e., $t_g' = \gamma t_g$ and $t_h' = \gamma t_h$): a) $\gamma = 1.0$, b) $\gamma = 0.5$, c) $\gamma = 0$. The transfer integrals and HOMO energies for **3** were used.

At this point the question is, given the similar topology of the crystal structures why do not all three of these phases undergo such a distortion and therefore have a metal–insulator transition? For a Fermi surface containing four warped open lines, like that in Figure 10c, the existence of a Fermi surface driven metal–insulator transition implies that one nesting vector allows the simultaneous superposition of the two lower and two upper lines. Given the inversion symmetry of the reciprocal space, this means that this mechanism is an interband nesting mechanism, exactly as it occurs in the blue bronzes.[22] For this mechanism to work, the warping of the two 1D components must be approximately the same. That this is possible, as shown in Figure 10c, despite the fact that the two step-chains are different (note that the actual transfer integrals a–f for **3** have been used in this simulation) is only because the two molecules have practically the same HOMO energy. Thus, at the limit of $\gamma = 0$, where they are only coupled by the small interactions a and b (which give the warping of the Fermi surface lines), the two bands are both half-filled. As our simulations, in which the energy difference between the HOMOs of molecules A and B has been increased, clearly show, when the filling of one band increases at the expense of the other, this is no longer true: the warping of the two types of lines starts to become different and thus the interband-nesting mechanism becomes more unlikely.[23] Thus, the water-containing salts cannot undergo a Fermi surface driven metal–insulator transition by the proposed mechanism without also having the HOMOs of the A and B molecules more alike. Thus, it is highly unlikely that this will occur in these latter systems. In conclusion, it seems that the separation of the closed and open portions of the Fermi surface, the possibility of a structure-induced metal–insulator transition, and the similarity of the HOMO energies of the two BEDT-TTF are intimately related for this series of systems.

All that remains now is to evaluate the likelihood that a small molecular motion might in fact lead to the destruction of the interactions g and h. A series of model calculations with BEDT-TTF dimers oriented as in interactions g and f as the starting point and then systematically changing the geometry, showed that indeed relatively small geometrical changes in the interaction could make these transfer integrals very weak. Simply speaking, when the two BEDT-TTF molecules become less coplanar, the π-type interaction in fact initially decreases, so that the transfer integral becomes very small, and increases again later when the σ-type interactions start to take over.[10] It thus seems that there are no structural reasons against the proposed interband nesting mechanism although, of course, the many degrees of freedom in these layers makes it impossible to give a firm answer concerning this point just on the basis of these calculations. However, they clearly suggest that the mechanism is plausible. The simplest way to test the proposed mechanism would be to carry out X-ray

  0947-6539/02/0817-3897 $ 20.00+.50/0

diffuse-scattering experiments.[24] If the interband nesting mechanism occurs, additional Bragg spots at ½c^* should exist below the transition temperature.

Finally, we should point out that, in view of the intrinsic disorder in many of these structures, it is not possible to rule out that the loss of the metallic properties for other systems of this series could be the result of an electronic localization. In fact, we believe that there is competition between the two types of mechanisms along the series. This feeling is reinforced when one remembers that these systems have two holes per four molecules and two molecules of each type in the repeat unit of the layer. Thus, it is clear that an increase in the difference in energy between the two HOMOs decreases the possibility of an interband-nesting mechanism; this increases the stability of the metallic state, but at the same time it also increases the possibility of an electron localization in one of the two different types of molecules of the lattice. For instance, our computations for the donor layers of **15** show that the separation between the closed and open parts of the Fermi surface is similar to that found for **1** and yet it loses its metallic character. In that case, the resistivity upturn is clearly less sharp than it is in **3**, and we are tempted to believe that the loss of the metallic behavior originates from electronic localization. As mentioned above, the relatively small but significant differences in the HOMO energies of the two BEDT-TTF in these salts is mainly associated with the terminal ethylenedithio groups, and the small geometrical changes that they induce, and not, as is more usual, with differences in the central carbon–carbon double bonds. Thus, even if electronic transport occurs within the donor layers, it is clear that the solvent and anion components of these salts have a strong control over the transport process through their intrinsic disorder and the way they control the HOMO energies of the two types of donors.

Different sets of pseudopolymorphs and electronic structure: Of course the geometrical differences between the two sets of pseudopolymorphs lead to differences in the individual $t_{\mathrm{HOMO\text{-}HOMO}}$ transfer integrals. However, as can be seen in Figure 6b and Figure 7d, in which we report the calculated band structure and Fermi surface for the donor layers of **19**, the differences are not really that significant (note that in contrast to all other systems we have considered so far, the β angle is here smaller than 90° and this leads to the "apparent" difference in the orientation of the closed part of the Fermi surface). Thus we shall not further elaborate on this issue and shall just state that there are no major differences in the electronic structures of the donor layers of the two sets of pseudopolymorphs. We only note that the separation between the closed and open parts of the Fermi surface is again large so that, according to our analysis, either a stable metallic state or a metal–insulator transition due to electron localization should be expected. In fact, the quite progressive loss of the metallic behavior is a strong argument in favor of electronic localization.

In conclusion, we propose that the electronic-band structures of all these systems are essentially identical, and that the key factor controlling the transport properties is the similarity, or difference, between the HOMO levels of the two BEDT-TTF molecules in the lattice. When this difference is very small, the metallic state can be unstable with respect to a structural modulation. As the HOMO energy difference increases, the stability of the metallic state toward the insulating modulated state increases but, very soon, the tendency toward an electronic localization also becomes strong. The complex interplay between the three situations seems to be essentially decided at the organic–inorganic interface.

Conclusion

An in-depth analysis of an homogeneous set of 21 accurate layered structures of metallic pseudopolymorphs of general formulation, β''-(BEDT-TTF)$_4$·(guest)$_n$·[$Re_6Q_6Cl_8$], (Q = S, Se) with diverse low-temperature behaviors, which differ solely by the nature of the solvent selectively included during the electrocrystallization process, has allowed the entangled issues of intermolecular interactions and Fermi surface topologies to be deciphered. We have revealed that a concerted balance of a precise set of weak intermolecular interactions at the organic–inorganic interface, none of which dominates any of the others, takes place upon substituting one guest molecule by another. The seemingly complex adjustment of the host electronic structure to the weak perturbation imposed by exchanging the guest molecules and balancing interfacial interactions can be thought of as an activation by up to 0.1 eV of the energy of the HOMO level of one of the two independent π-donor molecules A and B, while keeping the pattern of HOMO–HOMO intermolecular interactions in the layer essentially unaltered. It is concluded that, for essentially identical HOMO energies, that is, for $\alpha_A \approx \alpha_B$, the system is likely to experience an interband nesting leading to the occurrence of a metal-to-insulator phase transition at low temperature, as in the prototypical dioxane pseudopolymorph ($T_{MI} = 100$ K), whose metallic character is restored, however, at low temperature by the application of hydrostatic pressure. For small but significantly different HOMO energies, the nesting mechanism becomes less favorable, the structural transition is less likely to occur, and the metallic character becomes more stable. Meanwhile though, the two molecules A and B are different, and the susceptibility of one of them to become more oxidized is high. Hence, the transport data may then show evidence for competing localization phenomena in the form of a broad resistivity minimum, as is actually the case for most pseudopolymorphs. Remarkably then, the water phases remain metallic down to low temperature, either because the HOMO energies of the two independent BEDT-TTF molecules are not sufficiently different or because the interface is particularly well ordered, as indeed observed. With the exception of the dioxane phase, the resistivity upturns observed for the THF, CCl_4, $CHCl_3$, and pyridine phases are not very abrupt, a likely indication of localization phenomena.

Despite the tangible weakness of the concerted response to different guests of both the interfacial interactions and Fermi surface topology, in the end, having analyzed a sample of 21 very similar structures, it is a simple and convincing fact that such minute adjustments have sizeable manifestations on the

  0947-6539/02/0817-3898 $ 20.00+.50/0 *Chem. Eur. J.* **2002**, *8*, No. 17

macroscopic transport properties. One dominant tendency in the chemistry of molecular materials has been to explore many different structures associating many different π-donor molecules and ions of a variety of shape, volume, and charge to reveal diverse large structural and electronic effects that ultimately proved difficult to correlate. By contrast, we have demonstrated in this paper that keeping with one robust, single basic host structure and allowing for numerous tiny modifications, one discerns a concerted, inherently weak structural response of the system that is proportional to the magnitude of the underlying, equally weak activation of the HOMO energy of a fraction of the π-donor molecules within the slabs. One can then be confident that small variations on the intermolecular scale within ordered complex supramolecular systems, an issue of relevance to many current aspects in supramolecular chemistry,[25] are indeed responsible for comparatively larger collective electronic responses on the macroscopic scale.

Experimental Section

Materials: BEDT-TTF was prepared and purified as described earlier.[26] Crystals were grown by constant current oxidation of BEDT-TTF at a platinum-wire electrode.[4] $(Bu_4N^+)_2[Re_6Q_6Cl_8]^{2-}$ (Q = S, Se)[8] and $(Bu_4N^+)[Re_6S_5OCl_8]^{2-}$[27] were used as electrolytes and were prepared as described previously.

X-Ray diffraction studies: Data collection was performed at 293 K for all compounds, except for **17** (153 K), by using graphite monochromatized $Mo_{K\alpha}$ radiation on a STOE IPDS single-ϕ-axis diffractometer with a 2D area detector based on the Imaging Plate technology for all compounds, except **3** for which the data were collected on a κ-axis ENRAF-NONIUS CAD4-F diffractometer with a scintillation detector. The data for **3** were processed with XCAD4, and for all other compounds the images were processed with the set of programs from STOE.[28a] For all compounds an absorption correction was applied by using either semiempirical procedures based on an azimuthal psi-scan technique (compound **3**) or multiscan technique (compounds **2**, **6**, **9**, **12**, **13**, **16**, **18**, **19**) or numerical procedures based on face indexing (**1**, **5**, **8**, **10**, **11**, **14**, **15**, **17**, **20**, **21**). The structures were solved by direct methods and refined by full-matrix least-squares based on F^2, by using the program SHELX-97.[28b] All non-hydrogen atoms were refined anisotropically. The hydrogen atoms were simply included for all compounds in structure factor calculations at idealized positions, and assigned to ride on the atoms to which they were bound. X-ray data for all 19 structures are collected in Tables 1–5. CCDC-173636–173654 contain the supplementary crystallographic data for this paper. These data can be obtained free of charge via www.ccdc.cam.ac.uk/conts/retreiving.html (or from the Cambridge Crystallographic Data Centre, 12 Union Road, Cambridge CB2 1EZ, UK (fax: (+44) 1223-336-033; or e-mail: deposit@ccdc.cam.ac.uk).

Band-structure calculations: The tight-binding band structure calculations were based upon the effective one-electron Hamiltonian of the extended Hückel method.[29] The off-diagonal matrix elements of the Hamiltonian were calculated according to the modified Wolfsberg–Helmholz formula.[30] All valence electrons were explicitly taken into account in the calculations, and the basis set consisted of double-ζ Slater type orbitals for C and S and single-ζ Slater type orbitals for H. The exponents, contraction coefficients, and atomic parameters for C, S, and H were taken from previous work.[6] The transfer integrals were calculated according to the usual dimer splitting approximation.[31]

Acknowledgements

We thank Sandrine Perruchas for her contribution to the electrocrystallization experiments for **14** and **15**. This work was supported by the CNRS, the Région des Pays de la Loire, DGI-Spain (Project BFM2000-1312-C02-01), Generalitat de Catalunya (1999 SGR 207), and the joint French–Spanish Programs Picasso (1999–2000 01459 SF) and CNRS-CSIC (2000–2001 7944).

[1] K. Imaeda, J. Kröber, C. Nakano, M. Tomura, Y. Yamashita, H. Kobayashi, H. Inokuchi, A. Kobayashi, *Mol. Cryst. Liq. Cryst.* **1997**, *296*, 205.
[2] a) J. A. Schlueter, J. M. Williams, U. Geiser, J. D. Dudek, M. E. Kelly, S. A. Sirchio, K. D. Carlson, D. Naumann, T. Roy, C. F. Campana, *Adv. Mater.* **1995**, *7*, 634; b) J. A. Schlueter, J. M. Williams, U. Geiser, H. H. Wang, A. M. Kini, M. E. Kelly, J. D. Dudek, D. Naumann, T. Roy, *Mol. Cryst. Liq. Cryst.* **1996**, *285*, 43.
[3] S. Turner, P. Day, K. M. Abdul Malik, M. B. Hursthouse, S. J. Teat, E. J. MacLean, L. Martin, S. A. French, *Inorg. Chem.* **1999**, *38*, 3543.
[4] P. Batail, K. Boubekeur, M. Fourmigué, J.-C. P. Gabriel, *Chem. Mater.* **1998**, *10*, 3005.
[5] Unit cell data for $(BEDT\text{-}TTF)_2[Re_6S_6Cl_8]$: a) monoclinic phase: $a = 9.292(2)$, $b = 12.340(3)$, $c = 21.243(4)$ Å, $\beta = 97.33(3)^\circ$, $V = 2436.3(9)$ Å^3, $P2_1/n$, $Z = 2$; b) triclinic phase: $a = 9.333(2)$, $b = 10.962(2)$, $c = 12.709(3)$ Å, $\alpha = 80.63(3)$, $\beta = 97.33(3)$, $\gamma = 78.15(3)^\circ$, $V = 1210.3(4)$ Å^3, $P\bar{1}$, $Z = 1$. A. Deluzet, K. Boubekeur, P. Batail, unpublished results.
[6] A. Pénicaud, K. Boubekeur, P. Batail, E. Canadell, P. Auban-Senzier, D. Jérôme, *J. Am. Chem. Soc.* **1993**, *115*, 4101.
[7] J.-C. Gabriel, K. Boubekeur, P. Batail, *Inorg. Chem.* **1993**, *32*, 2894.
[8] J.-C. P. Gabriel, K. Boubekeur, S. Uriel, P. Batail, *Chem. Rev.* **2001**, *101*, 2037.
[9] When the crystals are grown in rigorously dried dimethylformamide solutions, the semiconducting ($\sigma_{300\,K} = 0.054\ S\,cm^{-1}$) monoclinic α phase, formulated α-$(BEDT\text{-}TTF)_4 \cdot (DMF)_2 \cdot Re_6S_6Cl_8$, is obtained instead. The latter proved to be identical to that described earlier[6] and formulated, m-$(BEDT\text{-}TTF)_4Re_6Se_5Cl_9 \cdot (DMF)$: C. Guilbaud, PhD Thesis, Nantes (France), **1998**.
[10] T. Mori, *Bull. Chem. Soc. Jpn.* **1999**, *72*, 2011.
[11] a) W. C. McCrone, *Physics and Chemistry of the Organic Solid State*, *Vol. 2* (Eds.: D. Fox, M. M. Labes, A. Weissberger), Interscience, New York, **1965**, p. 725; b) A. Nangia, G. R. Desiraju, *Topics in Current Chemistry, Vol. 198*, Springler, Berlin, **1998**, pp. 57–95.
[12] This estimate follows from the observation of a correlation between the volume of the calculated electron density envelope of a molecule and the molar volume of its liquid as discussed in: M. W. Wong, K. B. Wiberg, M. J. Frisch, *J. Comput. Chem.* **1995**, *16*, 385.
[13] a) M. H. Whangbo, M. Evain, J. J. Novoa, F. Mota, S. Alvarez, J. M. Williams, M. A. Beno, A. M. Kini, H. H. Wang, J. R. Ferraro, *The Physics and Chemistry and Organic Superconductors* (Eds.: G. Saito, S. Kagoshima). Springer, Berlin, **1990**; b) J. J. Novoa, M. H. Whangbo, J. M. Williams, *Mol. Cryst. Liq. Cryst.* **1990**, *181*, 25.
[14] A. Deluzet, P. Batail, Y. Misaki, P. Auban-Senzier, E. Canadell, *Adv. Mater.* **2000**, *12*, 436.
[15] P. K. Thallapally, A. Nangia, *CrystEngComm* **2001**, 114.
[16] G. R. Desiraju, T. Steiner. *The Weak Hydrogen Bond*, Oxford University Press, New York, **1999**.
[17] G. R. Desiraju, *Angew. Chem.* **1995**, *107*, 2541; *Angew. Chem. Int. Ed. Engl.* **1995**, *34*, 2311.
[18] a) E. Abrahams, P. W. Anderson, D. C. Licciardello, T. V. Ramakrishnan, *Phys. Rev. Lett.* **1979**, *42*, 673; b) E. Abrahams, S. V. Kravchenko, M. P. Sarachnik, *Rev. Mod. Phys.* **201**, *73*, 251.
[19] For a related study see: R. Rousseau, M.-L. Doublet, E. Canadell, P. P. Shibaeva, S. S. Khasanov, L. P. Rozenberg, N. D. Kushch, E. B. Yagubskii, *J. Phys. I France* **1996**, *6*, 1527.
[20] R. Rousseau, M. Gener, E. Canadell, unpublished results; M. Genez, PhD Thesis, University of Barcelona (Spain), **2002**.
[21] M.-H. Whangbo, J. Ren, W. Liang, E. Canadell, J.-P. Pouget, S. Ravy, J. M. Williams, M. A. Beno, *Inorg. Chem.* **1992**, *31*, 4169.
[22] a) E. Canadell, M.-H. Whangbo, *Chem. Rev.* **1991**, *91*, 965; b) M.-H. Whangbo, L. F. Schneemeyer, *Inorg. Chem.* **1986**, *25*, 2424.
[23] That the shape of the Fermi surface for a given band can change with the filling is very simple to understand by considering, for instance, the case of a pseudo-1D band its the energy minimum at Γ. Since the band

dispersion along one of the two reciprocal-space directions is larger than along the other, the Fermi surface will start being 2D for small fillings but will become pseudo-1D for larger fillings.
[24] R. Moret, J.-P. Pouget, *Crystal Chemistry and Properties of Materials with Quasi-One-Dimensional Structures*, (Ed.: J. Rouxel). Reidel, Dordrecht, **1986**, p. 87.
[25] D. M. Rudkevich, *Chem. Eur. J.* **2000**, *6*, 2679.
[26] J. Larsen, C. Lenoir, *Synthesis* **1989**, *2*, 134.
[27] S. Uriel, K. Boubekeur, P. Batail, J. Orduna, E. Canadell, *Inorg. Chem.* **1995**, *34*, 5307.
[28] a) STOE IPDS Software manual V2.87, December **1997**, STOE, Darmstadt, Germany; b) G. M. Sheldrick, SHELX-97, Programs for Crystal Structure Analysis, University of Gottingen, Germany.
[29] M.-H. Whangbo, R. Hoffmann, *J. Am. Chem. Soc.* **1978**, *100*, 6093.
[30] J. Ammeter, H.-B. Bürgi, J. Thibeault, R. Hoffmann, *J. Am. Chem. Soc.* **1978**, *100*, 3686.
[31] P. M. Grant, *J. Phys. (Paris)* **1983**, *44*, C3 – 847.

Received: December 4, 2001
Revised: April 19, 2002 [F3723]

  0947-6539/02/0817-3900 $ 20.00+.50/0